Edge Impurity Transport Study in Stochastic Layer of LHD and Scrape-off Layer of HL-2A

M. Kobayashi 1), S. Morita 1), C.F. Dong 1), Y. Feng 2), S. Masuzaki 1), M. Goto 1), T. Morisaki 1), H.Y.Zhou 1), H. Yamada 1) and the LHD experimental group 1)

1) National Institute for Fusion Science, Toki 509-5292, Japan
2) Max-Planck-Institute fuer Plasmaphysik, D-17491 Greifswald, Germany

Z. Y. Cui 3), Y. D. Pan 3), Y. D. Gao 3), P. Sun 3), Q. W. Yang 3) and X. R. Duan 3)

3) Southwestern Institute of Physics, P. O. Box 432, Chengdu 610041, China
E-mail contact of main author: kobayashi.masahiro@lhd.nifs.ac.jp

Abstract. Edge impurity transport has been investigated in the stochastic layer of LHD and the scrape-off layer (SOL) of HL-2A, as a comparative analysis based on carbon emission profile measurement and three-dimensional edge transport simulation. The 3D simulation predicts impurity screening effect in the both devices, but with different behavior against collisionality and the impurity source location. The difference is attributed to topological effects of the field lines in the stochastic layer and X-point poloidal divertor SOL. The carbon emission (CIV) profile in the stochastic layer of LHD shows clear signature of impurity movement towards downstream at high density range, in reasonable agreement with the 3D code simulation predicting impurity screening. Comparison of CIV profile measurements in HL-2A with the modelling is not straightforward, and a further assessment is necessary on the impurity source distribution/amount in the divertor plate and first wall, in order to interpret the experimental observations.

1. Introduction

Understanding of edge impurity transport is one of the most critical issues in magnetically confined fusion devices, in order to keep a purity of core plasma by reducing the impurity influx through LCFS (last closed flux surface), to identify material migration process and to control the impurity radiation pattern/intensity for achieving stable radiative/detached divertor operation. Divertor optimization to satisfy the required functions, heat load mitigation, control of impurity transport and the fuel/helium ash pumping, is still an open issue for future reactors. While the tokamak X-point poloidal divertor is being optimized in various aspects in the 2D axi-symmetric geometry [1], there is also another approach to explore a possibility of the large flexibility of 3D magnetic field geometry with symmetry breaking, which naturally occurs in the helical devices due to the coil configuration [2,3] or in the non-axisymmetric tokamaks with the externally applied resonant magnetic perturbation field [4,5,6]. The 3D configuration usually introduces stochasticity of magnetic field structure in the edge region, where one expects substantial difference in the transport properties compared to those in the axi-symmetric tokamak scrape-off layer, in terms of coupling between transport components of parallel and perpendicular to magnetic field lines. In this paper, we attempt to analyze the effects of the different magnetic field geometries on the edge impurity transport by comparing the stochastic layer of LHD (Large Helical Device) and the scrape-off layer (SOL) of HL-2A. The analyses are based on the carbon emission profile measurements with the EUV and VUV spectroscopy installed in LHD and HL-2A, and on the 3D edge transport code simulations implemented in the both devices.

2. Edge magnetic field structure and plasma parameter range in LHD and HL-2A

Fig.1 shows magnetic field structure and divertor configuration of LHD and HL-2A in terms of the connection length (L_C) distribution. LHD is a heliotron configuration with poloidal winding number of l=2 and toroidal field period of n=10. It has major radius of 3.9 m and averaged minor radius of ~ 0.7 m [2]. To realized a confinement magnetic field without net toroidal current, the two coils winds around the plasma helically in toroidal direction. This coil configuration creates stochastic magnetic field structure at the edge region due to the overlapping of magnetic island chains. The stochasticity introduces long connection length

flux tubes, more than 1 km, which interact with short flux tubes while traveling towards divertor plate. HL-2A tokamak has X-point poloidal divertor configuration with closed shape divertor chamber. The major radius is 1.65 m and minor radius is ~ 0.4 m, respectively [7]. The SOL consists of a bundle of flux tubes with L_C ~ 40 m.

One of the major differences in the transport characteristics between the LHD stochastic layers and HL-2A SOL is introduced by the contribution of perpendicular transport due to the magnetic field geometry. This effect is probably most pronounced in the parallel momentum transport. While in tokamak SOL, the total pressure is usually conserved along flux tubes unless we have significant charge exchange momentum loss at very low temperature. This pressure conservation provides the tight coupling between the downstream and upstream plasma condition, $T_{down} \propto n_{up}^{-2}$, $n_{down} \propto n_{up}^{3}$, which is called conduction limited regime and experimentally confirmed. In the stochastic layers, however, it is found that the coupling becomes rather modest [8,9],

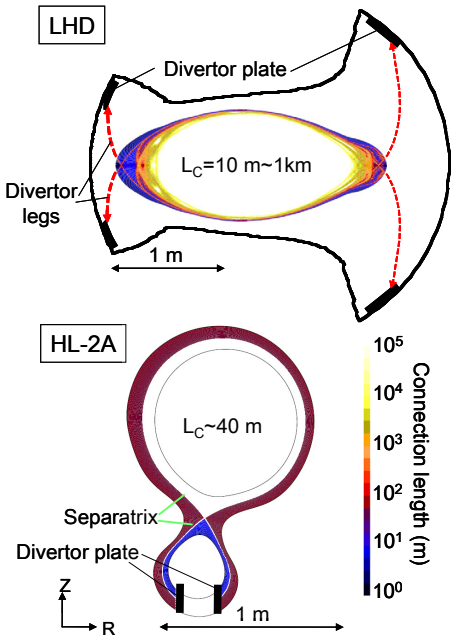

FIG.1 Connection length distribution and divertor configuration in LHD and HL-2A. The length is scaled with different colours.

$$T_{down} \propto n_{up}^{-1\sim-2/3}, n_{down} \propto n_{up}^{1\sim1.5}. \quad (1)$$

The 3D edge transport analyses have shown that this is due to the loss of parallel momentum, which is caused by the interaction between counter-acting parallel flows, resulting from the magnetic field topology in the stochastic field [9]. Such flow alternation is also measured in experiments [10]. While the conduction limited regime in tokamak SOL has an advantage to easily reach the dense and cold downstream plasmas, the modest dependence in the stochastic layer has an another advantage that the upstream can be brought into rather high density (collisionality) when the downstream becomes as dense and cold as in the tokamak SOL.

Fig.2 shows the range of edge plasma parameter (T_{eup}, n_{eup}) in the two devices. The upstream position is defined at the last closed flux surface (LCFS) on the outer mid-plane for HL-2A and outboard side edge surface layers (laminar region) for LHD. In the edge surface layers, the clustered long flux tubes are separated each other by short ones in a distance larger than the perpendicular transport scale, and thus starts to exhibit SOL-like parallel flow towards divertor. Contours of the SOL collisionality, $\nu^*_{SOL} \equiv L_{//} / \lambda_{ee}$, is also indicated, where λ_{ee} is the electron mean free path and $L_{//}$ is a characteristic scale length along magnetic field, which is either

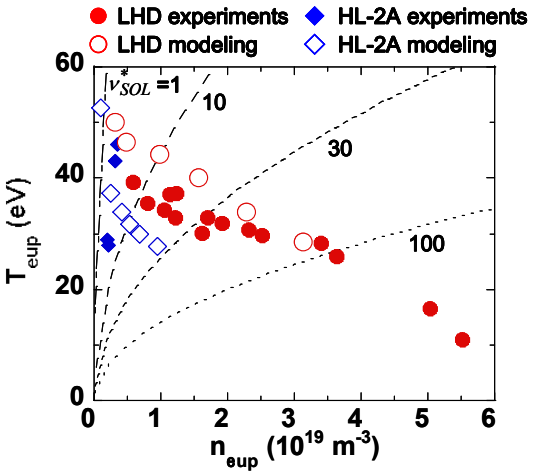

FIG.2 Edge plasma parameter range in LHD stochastic layer and HL-2A scrape-off layer. The lines indicate the SOL collisionality, ν^*_{SOL} (defined in the text). Circles and diamonds represent LHD and HL-2A data. Closed and open symbols indicate the data from experiments and modellings, respectively. The upstream location is taken at the edge surface layer at outboard side for LHD and at outboard mid-plane for HL-2A.

the half of L_C for HL-2A or the Kolmogolov length for LHD, both of them are estimated at about 20 m. For the present analyses, the NBI heated plasmas with 4 to 8 MW of LHD and the ohmic discharges with plasma current up to 380kA with input power up to300kW of HL-2A, have been compared. Unfortunately the experimental data of T_{eup} and n_{eup} in HL-2A is sparse, but the modeling results supplement the information. In the case of HL-2A, we have an upper boundary for the edge parameters around ν^*_{SOL}=20, where the computation indicates detachment onset. It is also consistent with experimental observation [11]. The access to the higher ν^*_{SOL}~100 in LHD before detachment onset is not only due to the higher heating power, but also due to the modest change of T_{down}, n_{down}, eq.(1), i.e. T_{down} decreases slowly against n_{up} as discussed above. The consequence of these features on the edge impurity transport is discussed in the next sections.

3. 3D edge transport modelling of LHD and HL-2A

In order to investigate the transport properties, we have implemented the 3D edge plasma transport code, EMC3[12]-EIRENE[13], in both LHD and HL-2A. EMC3 solves the fluid conservation equations of mass, parallel momentum, energy of electron & ion, together with impurity, in arbitral 3D geometry of magnetic field and divertor/first wall shape. The neutral recycling at divertor and first wall is treated by the kinetic transport model in EIRENE, which is also feasible in the 3D geometry. In the frame of fluid approximation, the parallel motion of impurity is considered to be in force balance in steady states as follows [14],

$$0 = -\frac{1}{n_z}\frac{\partial T_i n_z}{\partial s} + m_z \frac{V_{i//} - V_{z//}}{\tau_s} + ZeE_{//} + 0.71Z^2\frac{\partial T_e}{\partial s} + 2.6Z^2\frac{\partial T_i}{\partial s}, \qquad (2)$$

where T_z=T_i is assumed and $V_{i//}, V_{z//}, \tau_s, m_z$ being the parallel velocity of background ion and impurity, the slowing down time of impurity colliding with background ions, mass of impurity, respectively. The terms on the right hand side represent the impurity pressure gradient, friction force exerted by the background parallel plasma flow, electric field and electron & ion thermal force (temperature gradient force), respectively. s is the coordinate along the magnetic field. In perpendicular direction, pure diffusion is assumed and the diffusion coefficient is set to be same as those of background plasma. As often discussed, the dominant forces in the equation are the friction force and the ion thermal force, the second and the forth terms on the right hand side. Since usually the background plasma flow is directed towards divertor plates, the friction force sweeps the impurity to the divertor region, while due to the $\nabla_{//}T$ which directs towards upstream the thermal force pushes impurity to the upstream direction. In the both devices, the divertor plates are made of graphite and it is the main source of carbon, which is an impurity species treated in the present modelling. The

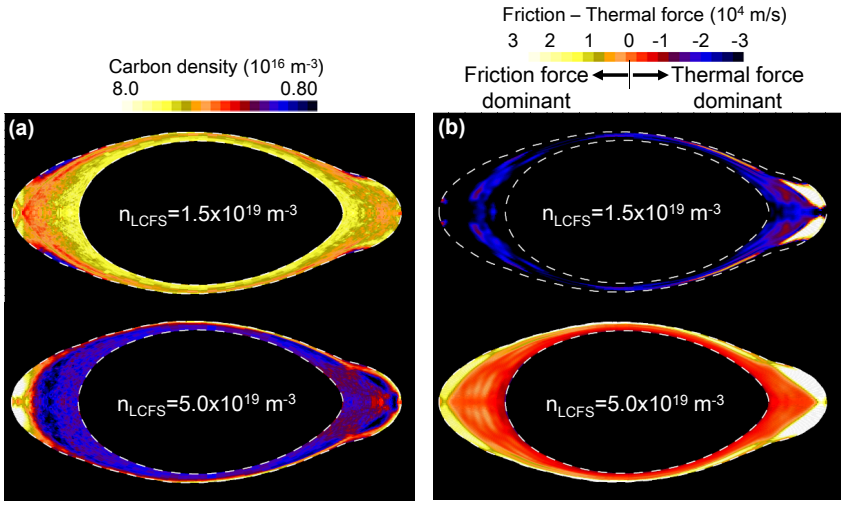

FIG.3 (a) carbon density distribution in LHD for different n_{LCFS} obtained by the 3D modellings. (b) Friction-Thermal force balance as explained in eq.(3). The yellow and black colours represent friction force and thermal force dominant region, respectively. The dashed lines indicate computation boundary. n_{LCFS} corresponds to 2~3×n_{up} of Fig.2.

neutral impurity source from the divertor plate is distributed according to the plasma particle deposition pattern with a certain sputtering coefficient, C_{sput}. For the present analysis, C_{sput} is a free parameter and fixed to 2% for LHD while for HL-2A it has to be changed to get agreement with the experiments, as discussed later. The ejection energy from the material surface is set to be 0.05 eV for all cases. Although the rather complex dissociation process of hydrocarbon is beyond the scope of this paper, the major results of the analyses will not change even if the injection energy is changed.

Resulting carbon density distribution in LHD is plotted in Fig.3 together with the friction-thermal force balance,

$$V_{z//} \approx V_{i//} + \frac{\tau_s}{m_z}\left(2.6Z^2\frac{\partial T_i}{\partial s} + 0.71Z^2\frac{\partial T_e}{\partial s}\right), \qquad (3)$$

where the electric field and pressure gradient terms are neglected because they are usually small. At the low density, n_{LCFS}=1.5x10^{19} m^{-3}, the carbons are distributed around the LCFS, Fig.3 (a) (upper), due to the large inward velocity caused by the thermal force as shown in Fig.3 (b) (upper), where the almost entire region is covered by the thermal force dominant region except for the outboard edge. At the high density, n_{LCFS}=5.0x10^{19} m^{-3}, on the other hand, the carbons are pushed back to the periphery, due to the increasing friction force, Fig.3 (b) (lower), resulting in the impurity screening, as shown in Fig.3 (a) (lower). It is noted that the friction dominant region is distributed in all poloidal direction surrounding the stochastic layer. This provides effective screening for the impurity coming from all directions.

The results of HL-2A are plotted in Fig.4 for the different density cases. Similarly to the LHD case, the higher density leads to the impurity screening. At the low density case, the region above the X-point is deeply in the thermal force dominant while the near the divertor plate is friction dominant. In spite of the dominant friction force near the divertor plates, any small leakage of impurity out of the friction dominant region builds up at the upstream due to the strong thermal force above X-point. Increasing density strengthens the friction force near divertor plate and weakens the thermal force above X-point. This gives rise to a good screening. However, it is also noted that the residual thermal force can not be removed completely around/above X-point at the highest density just before the detachment transition, as shown in Fig.4 (b) (lower). This indicates that the SOL is relatively weak to the impurity injected around upstream, i.e. impurity source at the first wall.

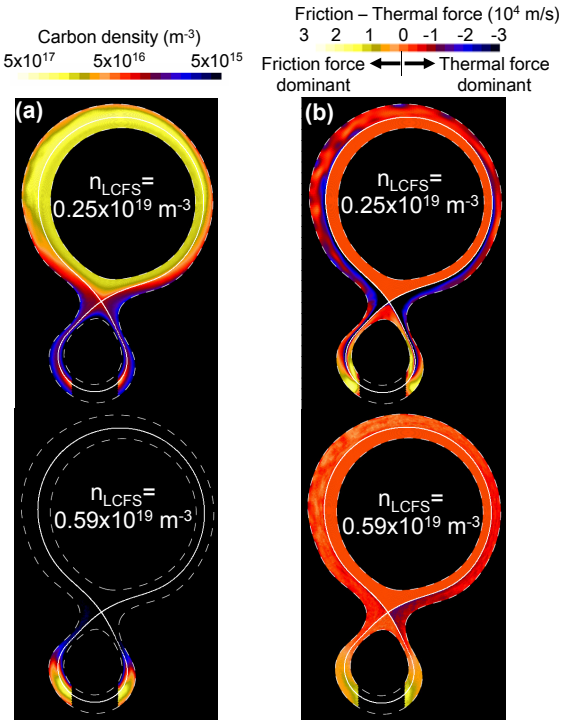

FIG.4 (a) carbon density distribution in HL-2A for different n_{LCFS} obtained by the 3D modellings. (b) Friction-Thermal force balance as explained in eq.(3). The yellow and black colours represent friction force and thermal force dominant region, respectively. The white solid lines and the dashed lines indicate separatrix and computation boundaries, respectively.

As a measure of degree of the screening, the ratio, $n_{up}^{imp}/n_{dowm}^{imp}$, is plotted in Fig.5 against ν_{SOL}^{*}, where n_{up}^{imp} and n_{dowm}^{imp} are the impurity density at upstream (LCFS) and near divertor plates, respectively, summed up over all charge states. When the ratio becomes below unity, it can be considered that the screening starts. The impurity source is

distributed not only at the divertor plate but also at the first wall uniformly for the both devices to see the effect of source location. In HL-2A, the ratio decreases rapidly above ν^*_{SOL} ~5, down to 0.1 showing strong screening against the divertor source. This is understood as due to the strong dependence, $T_{down} \propto n_{up}^{-2}$, $n_{down} \propto n_{up}^{3}$, which brings the downstream SOL to deeply in the friction dominant regime, where the parallel flow towards divertor plate is available driven by the sink action at the target, and also due to the closed divertor structure where the impurity has fewer chance to escape as neutrals. On the other hand, it is found that the HL-2A SOL has almost no screening effect against the first wall source, as anticipated from Fig.4 (b) (lower). This is again related to the strong dependence of T_{down} and n_{down}, which brings the divertor plasma to detachment regime while the upstream remains at rather low ν^*_{SOL}. Also, almost no flow acceleration is available at the upstream in the frame of the present model, in which the driver of the flow is only the ionization source and the sink action at the divertor plates, both of them are localized near divertor region.

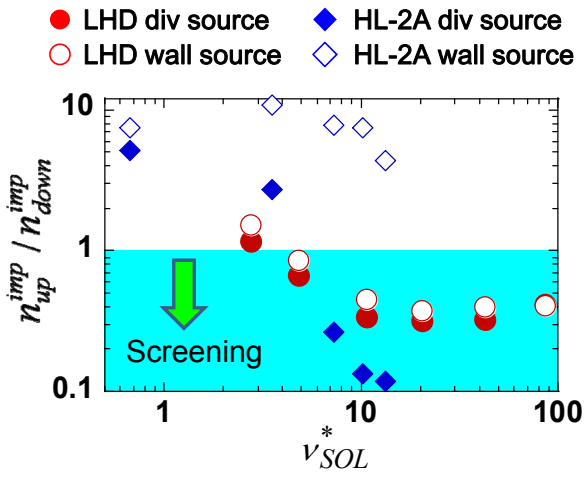

FIG.5 Impurity screening effect measured by the ratio $n_{up}^{imp} / n_{dowm}^{imp}$ obtained in modelling. The smaller the value is, the larger the screening effect. Circles for LHD, diamonds for HL-2A. Closed and open symbols represent divertor source and first wall source, respectively.

In the case of LHD, the stochastic layer has screening effect against both divertor and first wall source, although the reduction of the ratio is not as large as those of HL-2A. The smaller screening effect than the HL-2A is considered due to the open divertor structure as shown in Fig.1, in which case the neutral impurity has more chance to reach the upstream plasmas, which has less screening effect than the downstream. The screening effect against the first wall source is explained by the combination of the following processes: the modest dependence, $T_{down} \propto n_{up}^{-1\sim-2/3}$, $n_{down} \propto n_{up}^{1\sim1.5}$ helps the upstream goes to higher ν^*_{SOL}, i.e. higher density as discussed above. Due to the dependence of eq.(1), the downstream density is relatively low and never exceeds the upstream density [8,9]. This allows the recycling neutrals to escape from the divertor region, penetrating deep in the edge region. The current open divertor configuration in LHD also helps the recycling neutrals escape from the divertor region. This gives rise to substantial upstream ionization source, which provides flow acceleration towards divertor. At the inner radial location, the remnant islands exist with very small ratio, $B_r / B_t \sim 10^{-4}$, where B_r and B_t are radial and toroidal magnetic field. When the edge plasma parameters satisfy the condition [15],

$$n / T^{5/2} > \Theta^2 \kappa_{//0} / \chi_{\perp}, \qquad (4)$$

here $\kappa_{//0}$ and $\chi_{\perp}$ are parallel heat conductivity coefficient and perpendicular heat conductivity, respectively, and $\Theta \approx B_r / B_t$, the enhanced perpendicular energy transport channel, $n \chi_{\perp} \partial T / \partial r$, starts to compensate the parallel ones along the braiding magnetic fields. For the value of $\Theta \sim 10^{-4}$, the ion energy transport easily satisfies the eq.(4) in the LHD stochastic layer. This process avoids developing large $\nabla_{//} T$, i.e. thermal force, at high

collisionality. Since the $\frac{friction\ force}{thermal\ force} \propto \frac{M n_i}{|\nabla_{//} T_i| T_i}$ with M being Mach number, the above three process favors larger friction force dominating over the thermal force. This is the reason for the formation of the friction dominant region at the upstream, resulting in the impurity screening against the both first wall and divertor plate sources. The analysis shows that the perpendicular interaction of flux tubes in the stochastic layer alters the plasma characteristics, and provides different behaviors of impurity screening effect against ν^*_{SOL} and the source location.

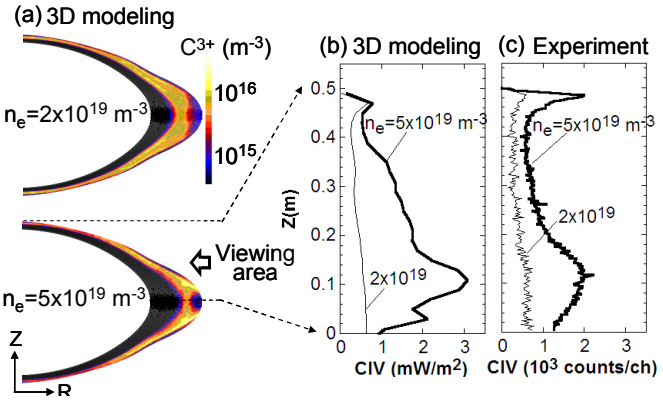

FIG.6 (a) C^{3+} carbon density (emitting CIV) distribution obtained by the modelling in LHD, and chord-integrated CIV profiles obtained by (b) modelling and (c) experiments for two different densities, as a function of vertical coordinate, Z.

4. Experimental observation

VUV, EUV spectroscopy systems have been installed in LHD [16] and in HL-2A [17] respectively, in order to investigate edge impurity transport. Fig.6 (a) shows the C^{3+} carbon density distributions for the low and high density cases (n_{LCFS}=2.0 and 5.0x10^{19} m^{-3}), where the edge region changes from thermal force dominant to friction force dominant regime, as indicated by the modelling. At the low density case the C^{3+} carbon distributes almost uniformly in poloidal direction as seen in Fig.6 (a) (upper). At the high density case, on the other hand, the screening effect pushes impurity towards the flux tubes of divertor legs, resulting in strong poloidal modulation of the distribution as shown in Fig.6 (a) (lower). The change is reflected on the vertical profile of the line integrated CIV (1548 Å) emission in horizontal view. Profiles obtained from the modelling results are plotted in Fig.6 (b), where one sees a clear change of the profiles from a flat to peaked one with increasing density. The peak around Z=0.1 m corresponds to the location of divertor legs. Similar change of the emission profiles with increasing density is observed in the experiments obtained in the same viewing area, as shown in Fig.6 (c). Emission of CIII (977 Å), CIV and CV (40.27 Å) was also measured at density scan. The density dependence of the each line emission was analyzed using the 3D edge transport code when the screening occurs, using the same viewing area as the experiments. Here the intensity of CIII and CIV are interpreted as a proxy for the source, and CV as a proxy for the impurity at deeper radial position. It is found that the behavior of measured emission agrees well with the model prediction with impurity screening [9, 18], i.e. slight increase of CIII and CIV, decrease of CIV against density scan. From these results, at the moment qualitative trend of screening is confirmed in LHD.

In HL-2A, line integrated CIV profile measurements have been conducted. The obtained profiles are plotted in Fig.7, together with the viewing angle of the spectroscopy shown in the right figure. Z coordinate starts at the center of plasma and increases downward. At the very low density, profile becomes almost flat in Z direction. In terms of the modelling, this is interpreted as due to the distribution of CIV emission which is almost uniform but slightly intense at the inboard side (Fig.7 (c) (upper)) that contributes to make the profile flat. In this low density case, the thermal force is dominant above X-point, as shown in Fig.4 (b) (upper), and is stronger at the outboard side than at inboard side because of the in-out asymmetry of the configuration, i.e. the shorter field line length from divertor to mid-plane at outboard side, and larger energy flux though LCFS is assumed at the outboard side due to the narrower flux

surface distance (Shafranov shift). This gives rise to the in-out asymmetry of the thermal force and of the impurity density distribution, which is larger at inboard side. Increasing density leads to the peaked CIV profile around Z=0.35 m in experiments with the concomitant increase of emission itself. In the modelling, the peak also appears at high density but the location is shifted outward, Z=0.40 m. The peak comes from the localized emission around X-point as shown in Fig.7 (c) (lower), which is caused by the screening effect at high density. As for the deviation of the peak location, we need further careful check of the reconstruction of magnetic flux surface and the calibration of the viewing lines of experiments and modelling. It is found that, in order to reproduce the increased emission with increasing density observed in the experiments, it is necessary to increase the impurity source from the divertor, i.e. sputtering coefficient from 1% to 10%, as indicated in Fig.7 (b). On the other hand, introducing first wall source (10% of divertor source, distributed uniformly) gives rise to a flat profile as shown in Fig.7 (b) with dashed line, due to the residual thermal force above X-point as discussed in section 3, although the measured profile always peaked at high density. The comparison between the experimental data and the modelling implies either that, there is additional impurity source other than the divertor sputtering, or that there exists another screening effect above X-point, which is not included in the present modelling such as large poloidal flow formation as observed and analyzed in tokamak devices [19, 20], if the first wall source is assumed to explain the emission increase in the experiments.

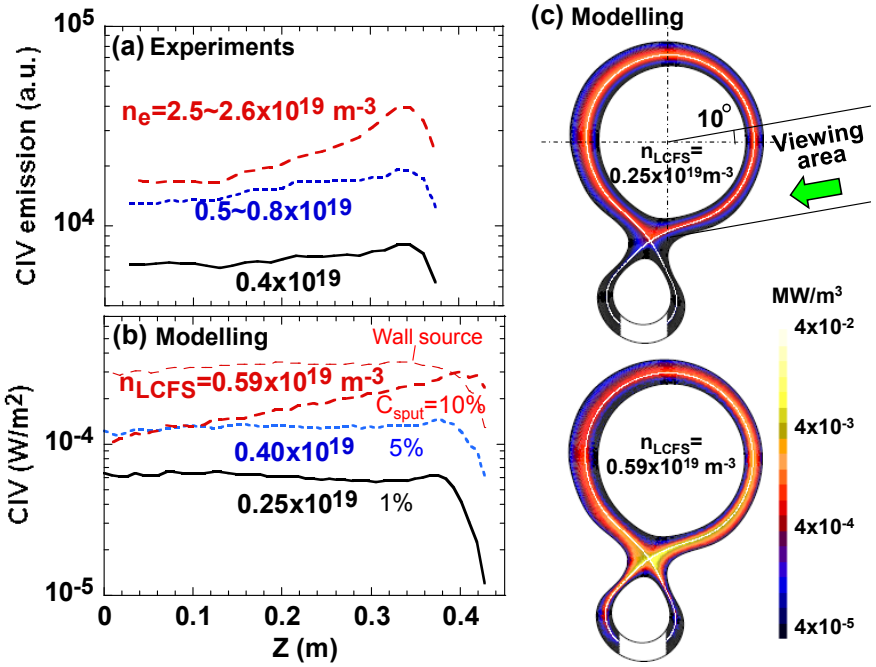

FIG.7 Line integrated CIV profiles obtained in HL-2A for different densities. (a) Experiments, (b) Modelling, (c) CIV distribution obtained by the modelling together with viewing area of spectroscopy. In the modelling, sputtering coefficient is varied as indicated in (b). The result of first wall impurity source is shown by dashed line in (b).

5. Summary

In order to address the effect of magnetic field geometry on the edge impurity transport, the comparative transport analyses between the LHD stochastic layers and the HL-2A SOL have been conducted, both of them have distinct magnetic field structure each other in terms of the connection length and the flux tube topology. The 3D edge transport code EMC3-EIRENE has been implemented for the both machines, and the profile measurements of carbon emission have been performed using the EUV, VUV spectroscopy in the both devices. Comparison of the simulation results shows clear difference in the screening process between LHD and HL-2A. In the HL-2A, the strong screening effect appears suddenly above ν^*_{SOL}~5 for divertor impurity source. But there is almost no screening effect against the first wall source due to the residual thermal force at the upstream (above the X-point) even at the

highest density just before detachment onset. In the case of LHD, the screening also appears above ν^*_{SOL}~5, where the effect seems to be weaker than those of HL-2A. The screening is, however, available also for the first wall source. This is due to the enhanced perpendicular transport in the stochastic layer, which can bring the entire upstream region into friction dominant regime.

The comparison of the modelling with the spectroscopy measurements shows, at least, a qualitative agreement in LHD in terms of the CIV emission profiles and CIII, CIV, CV intensity against density scan, indicating the existence of the screening effect. In the HL-2A case, the interpretation of the experimental data in terms of the present impurity transport model is not complete. We still need further analysis, on the comparison of CIV peak location appeared in both experiments and modelling, on the impurity source distribution/amount in the divertor and first wall.

For understanding the impurity transport properties in the different magnetic field geometry in LHD and HL-2A, and for validating the model prediction obtained in the present analyses, not only in the qualitative behavior but also in quantitative behavior, we need further systematic and organized experiments between LHD and HL-2A.

Acknowledgements

The authors wish to thank the LHD and HL-2A operation group for their excellent technical support. The authors are grateful for the support for the computational resources: Plasma Simulator SR16000 L2 powered by HITACHI Ltd, and AMD Opteron-InfiniBand Cluster Machine, by Grant-in-Aid for Science Research on Priority Areas (Area 465, No.18070005) from MEXT Japan. The computational work is partly supported by the NIFS budget code NIFS10ULPP016. This work was partly supported by the JSPS-CAS Core-University Program in the field of "Plasma and Nuclear Fusion".

References

[1] *"Progress in the ITER physics Basis: Chapter 4 : Power and particle control"*, Nucl. Fusion **47** (2007) S203.
[2] OHYABU, N. et al., Nucl. Fusion **34** (1994) 387.
[3] GRIGULL, P. et al., Plasma Phys. Control. Fusion **43** (2001) A175.
[4] GHENDRIH , PH. et al., Nucl. Fusion, **42** (2002) 1221.
[5] FINKEN , K.H. et al., Nucl. Fusion **47** (2007) 522.
[6] EVANS, T. et al., Nature Phys. **2** (2006) 419.
[7] YANG, Q.W. et al., Nucl. Fusion **47** (2007) S635.
[8] MASUZAKI, S., et al., J. Nucl. Mater. **313-316** (2003) 852.
[9] KOBAYASHI, M. et al., Fusion Sci. Technol. **58** (2010) 220.
[10] EZUMI, N. et al., J. Plasma Fusion Res., **8** (2009) 429.
[11] YAN, L.W. et al., J. Nucl. Mater. **390-391** (2009) 246.
[12] FENG, Y. et al., Contrib. Plasma Phys. **44** (2004) 57.
[13] REITER, D. et al., Fusion Sci. Technol. **47** (2005) 172.
[14] STANGEBY, P.C., and ELDER, J.D., Nucl. Fusion **35** (1995) 1391.
[15] FENG, Y. et al., Nucl. Fusion, **46** (2006) 807.
[16] DONG, C.F. et al., Rev. Sci. Instrum. **81** (2010) 033107.
[17] CUI, Z. et al., Rev. Sci. Instrum. **81** (2010) 043503.
[18] KOBAYASHI, M. et al., Proceedings of 22nd IAEA FEC (13-18th Oct. 2008, Geneva), EX/9-4. http://www-pub.iaea.org/MTCD/Meetings/fec2008pp.asp
[19] ASAKURA, N. and ITPA SOL and Divertor Topical Group, J. Nucl. Mater. **363-365** (2007) 41.
[20] TAKIZUKA, T. et al., Nucl. Fusion **49** (2009) 075038.